Research Article
Vol. 10, No. 5 / May 2023 / Optica 619

OPTICA

Single-shot quantitative amplitude and phase imaging based on a pair of all-dielectric metasurfaces

Qianyi Wu,[1,†] Junxiao Zhou,[1,3,†] Xinyu Chen,[1] Junxiang Zhao,[1] Ming Lei,[1] Guanghao Chen,[1] Yu-Hwa Lo,[1] and Zhaowei Liu[1,2,*]

[1]Department of Electrical and Computer Engineering, University of California San Diego, 9500 Gilman Drive, La Jolla, California 92093, USA
[2]Materials Science and Engineering Program, University of California San Diego, 9500 Gilman Drive, La Jolla, California 92093, USA
[3]juz095@ucsd.edu
[†]These authors contributed equally to this work.
*zhaowei@ucsd.edu

Received 13 December 2022; revised 19 April 2023; accepted 20 April 2023; published 17 May 2023

Quantitative amplitude and phase imaging (QAPI) has been an effective technique to examine label-free biomedical samples. Simple and reliable QAPI techniques realized by replacing conventional bulky optical elements with planar structures will improve the system portability and facilitate in vivo imaging applications. Here, we propose a single-shot QAPI method realized by simply inserting a pair of all-dielectric geometric phase metasurfaces into a traditional microscope. The first metasurface splits a linearly polarized incident beam into two circularly polarized components and the following metasurface deflects the two beams back toward their initial directions. The metasurface pair generates two laterally displaced replicas of the input object, of which the interference forms a retardance image with a bias retardation controlled by an analyzer. The amplitude and phase information of the object is reconstructed from four retardance images simultaneously recorded by a polarized camera. The metasurface pair can be placed near any conjugate plane of the object, which provides a flexible and robust configuration for QAPI, demonstrating its wide usage in live imaging.

https://doi.org/10.1364/OPTICA.483366

1. INTRODUCTION

Phase information of many specimens are appealing to biologists and material scientists. Traditionally, label-free imaging techniques such as Zernike phase-contrast microscopy [1] and differential interference contrast microscopy [2] can qualitatively reveal the phase profiles of samples without suffering from phototoxicity, photobleaching, or blinking or saturation [3,4]. To quantitatively characterize weakly absorbing and scattering objects, a variety of quantitative phase imaging (QPI) techniques have been proposed [5,6], including phase-shifting interference microscopy [7], transport of intensity equations [8], Fourier ptychography [9,10], digital holographic microscopy [11], diffraction phase microscopy [12], white light quantitative imaging unit [13], quadriwave lateral shearing interferometry [14,15], and quantitative fourth-generation optic microscopy [16]. These approaches have shown success in various applications, although trade-offs must be made among the resolution, field of view (FOV), sensitivity, and acquisition rate to accommodate different scenarios [5].

Metasurfaces consisting of planar subwavelength structures with desired arrangement display properties are not found in naturally occurring materials [17,18]. The capability of arbitrary wavefront manipulation and desirable multifunctionality distinguish metasurfaces in a wide range of applications, such as metalens [19–22], holograms [23,24], augmented reality [25,26], and analog computing [27–29], including spatial differentiation [30–32]. In the past several years, metasurface-assisted QPI as well as quantitative phase gradient imaging (QPGI) methods have been demonstrated [33–36]. They provide a comparable space-bandwidth product and phase sensitivity in traditional methods, while largely simplifying the conventional bulky systems by leveraging the compactness and high compatibility of metasurfaces. As trade-offs, these techniques are typically accompanied with certain limitations, such as time-consuming reconstruction, a high fabrication accuracy requirement or a tight positioning tolerance. A computation-light, fabrication-friendly, and alignment-insensitive QPI method with a compact configuration and single-shot capability is highly desired.

In this work, we propose and experimentally demonstrate a single-shot quantitative amplitude and phase imaging (QAPI) technique based on a pair of all-dielectric geometric phase metasurfaces, which can be placed anywhere near the conjugate planes of the object in the optical path of a conventional microscope. The proposed metasurfaces separate and recombine the two circularly polarized components of a linearly polarized incident wavefront with a lateral displacement that can be tuned by the distance between the two metasurfaces. The phase retardation between the two replica images is controlled by the metasurface periods and the orientation of the linear analyzer. The quantitative amplitude and phase information of the object can be reconstructed from four retardance images with different phase retardations captured simultaneously by a polarized camera. We demonstrate the QAPI capability of the metasurface pair with both unstained and stained biological samples. The proposed metasurfaces can be inserted into any existing polarized imaging system for real-time QAPI imaging without any other modifications.

2. METHODS

The core idea of the proposed QAPI method is to use a pair of geometric phase metasurfaces [37,38] to encode the amplitude and phase information of an object in differential interference patterns. Figure 1(a) depicts the schematic of the metasurface-based QAPI. The x-polarized input beam $E_{\mathrm{in}}(x, y)$ passing through a polarizer (P) successively illuminates metasurfaces MS_1 and MS_2 with displacements of z_1 and z_2 with respect to the object. The geometric phase metasurfaces permute the polarization states of the left- and right-handed circularly polarized (LCP and RCP) components of the incident beam, while introducing a geometric phase of $+2\varphi_i$ $(-2\varphi_i)$ to the LCP (RCP) beam, respectively. Here, $\varphi_i(x, y) = \pi(x - \xi_i)/\Lambda_i$, $i = 1, 2$ are the designed orientations of the local optical axes of the two metasurfaces, ξ_i is the transverse shift of MS_i along x axis, and Λ_i is the period of MS_i. The corresponding phases introduced to the LCP and RCP beams are shown in Fig. 1(b). The first metasurface MS_1 splits the two circularly polarized components of the input beam into different propagation directions with angles of $\pm\arcsin(\lambda/\Lambda_1)$ with respect to the z axis, while the second metasurface MS_2 reverses the polarization handedness of the two replicas and deflects them by angles of $\mp\arcsin(\lambda/\Lambda_2)$ back toward their original directions. The two circular-polarization-sensitive metasurfaces modulate the transmitted light so that the output of the imaging system is equivalent to the image of an effective object with electric fields for LCP and RCP components as

$$E^{L,R}_{\mathrm{in;eff}}(x, y) = \exp\left[\mp j2\pi\left(\frac{\xi_1}{\Lambda_1} - \frac{\xi_2}{\Lambda_2}\right)\right] \times \exp\left[-j\pi\lambda\left(\frac{z_1}{\Lambda_1^2} - \frac{2z_1}{\Lambda_1\Lambda_2} + \frac{z_2}{\Lambda_2^2}\right)\right] \times E_{\mathrm{in}}\left(x \pm \left[\lambda\left(\frac{z_1}{\Lambda_1} - \frac{z_2}{\Lambda_2}\right)\right], y\right) \times \exp\left[\pm j2\pi\left(\frac{1}{\Lambda_1} - \frac{1}{\Lambda_2}\right)x\right] |L, R\rangle, \quad (1)$$

where $|L, R\rangle$ are the LCP and RCP bases represented with Dirac bracket notation. See Section S1 of Supplement 1 for details.

To obtain the interference of the two orthogonally polarized replicas, an output linear analyzer (A) is used. For simplicity, we assume the imaging system has a magnification of unity. By projecting the LCP and RCP components in Eq. (1) onto the analyzer with the axis of transmission Θ with respect to x axis and add them up, the output electric field turns out to be the sum of two laterally displaced images with opposite phase retardation, so

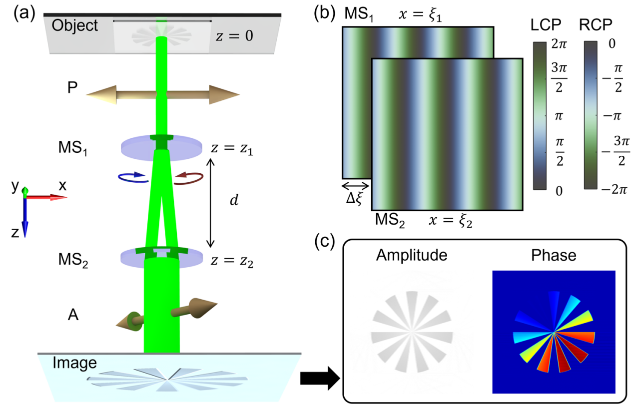

Fig. 1. Schematic of the metasurface-based QAPI along with its operation principle. (a) Schematic of the complex amplitude imaging employing two metasurfaces with distances z_1 and z_2 with respect to the object. P, polarizer; MS, metasurface; and A, analyzer. (b) Designed geometric phases of two metasurfaces with the same period and a relative displacement of $\Delta\xi$ along the x axis. The LCP and RCP light obtain phases with opposite signs. (c) Amplitude and phase of the object reconstructed given a series of retardance images.

$$E_{\mathrm{out}}(x_3, y_3) = C\left\{\begin{array}{l} E_{\mathrm{in}}(x_3 - \Delta, y_3)\exp[j(\kappa(x_3) + \psi - \Theta)] \\ +E_{\mathrm{in}}(x_3 + \Delta, y_3)\exp[-j(\kappa(x_3) + \psi - \Theta)] \end{array}\right\}, \quad (2)$$

where C is a constant phase term, $\Delta = \lambda z_2/\Lambda_2 - \lambda z_1/\Lambda_1$ is a lateral displacement, $\kappa(x) = 2\pi(1/\Lambda_1 - 1/\Lambda_2)x$ is a space-variant phase resulted from the period difference of the two metasurfaces, and $\psi = 2\pi(\xi_1/\Lambda_1 - \xi_2/\Lambda_2)$ is a bias retardation.

Generally, the space-variant phase $\kappa(x)$ leads to a sinusoidal background in the interference image. For the special case of two metasurfaces with an identical period Λ, MS_2 perfectly cancels the opposite tilted phases of LCP and RCP beams gained from MS_1, which leads to an output intensity as

$$I_{\mathrm{out}}\left(x_3, y_3, 2\theta'\right) \sim \left|E_{\mathrm{in}}(x_3 - \Delta_0, y_3)\exp\left(j\theta'\right) + E_{\mathrm{in}}(x_3 + \Delta_0, y_3)\exp\left(-j\theta'\right)\right|^2, \quad (3)$$

where $\Delta_0 = \frac{\lambda d}{\Lambda}$ is the lateral displacement, $d = z_2 - z_1$ is the distance along the z axis between the two metasurfaces, $\theta' = \frac{2\pi\Delta\xi}{\Lambda} - \Theta$ is the bias retardation, and $\Delta\xi = \xi_1 - \xi_2$ is the relative displacement of the metasurfaces along the x axis.

Thus, by using a polarized camera with interlaced micropolarizers of orientation $\alpha_i = (i - 1) \times \pi/4$, four retardance images $I_i = I_{\mathrm{out}}(x_3, y_3, (i - 1) \times \pi/2)$ can be obtained simultaneously (assume $\Delta\xi = 0$), with which the complex transmittance of the sample is reconstructed, as shown in Fig. 1(c). For a complex object $E_{\mathrm{in}}(x, y) = A(x, y)\exp[j\phi(x, y)]$, when the lateral displacement Δ_0 is small, the unidirectional phase gradient can be calculated with a four-step phase-shifting method as [39]

$$G_x \approx \frac{1}{2\Delta_0}[\phi(x_3 + \Delta_0, y_3) - \phi(x_3 - \Delta_0, y_3)] = \frac{1}{2\Delta_0}\mathrm{atan}\left(\frac{I_2 - I_4}{I_1 - I_3}\right). \quad (4)$$

For the general case when the two metasurfaces have different periods, the phase gradient of the objects can still be calculated in a similar manner with an estimation of local phase retardations and a generalized phase-stepping method [40]. Phase reconstruction by simply integrating experimentally captured unidirectional QPGI images generally produces undesired linear artifacts along the shearing direction [41]. Here, to avoid the noise-induced artifacts, we exploit the fact that the second-order partial derivative of the object phase along the y direction is sparse [42]. Recovering the phase from the phase gradient along the x direction is equivalent to solving a Poisson equation [43]. We then enforce the sparsity as a prior and solve the l_1 total variation regularized optimization problem

$$\min_{\phi,\nu} \frac{1}{2}\left\|\partial_x^2\phi - \partial_x G_x\right\|_2^2 + \mu\|v\|_1$$
$$\text{s.t.}\, \nu = \partial_y^2\phi, \tag{5}$$

where μ is the tuning parameter for the prior, and v is an auxiliary variable. We solve the problem with the alternating direction method of multipliers (ADMM) algorithm [44]; see Section S2 of Supplement 1 for details. The regularized reconstruction allows us to achieve artifact-free QPI with a single shot measurement. The reconstruction typically requires 10 iterations. For a 1000×1000 image, the computation takes about 4 s on a desktop with a i7-11700 K CPU using MATLAB.

The amplitude of the object is approximated by

$$A(x_3, y_3) \approx \sqrt{A(x_3-\Delta_0, y_3)\, A(x_3+\Delta_0, y_3)}$$
$$= \sqrt{\frac{|I_1 - I_3| + |I_4 - I_2|}{4(|\cos 2\Delta_0 G_x| + |\sin 2\Delta_0 G_x|)}}. \tag{6}$$

3. EXPERIMENTAL RESULTS

A. Fabrication and Characterization of the Metasurfaces

To demonstrate the proposed concept, we designed three dielectric metasurfaces that were then fabricated by a laser writing method (Altechna R&D). The photographs of two metasurface pairs with periods of 8 mm, 1 mm, and identical periods of 1 mm are shown in Figs. 2(a) and 2(d), respectively. These metasurfaces are fabricated inside the bulk SiO_2 substrates 80 µm away from the top surfaces. When an intense femtosecond pulse laser beam illuminates the substrate, the SiO_2 will partially decompose into porous glass $SiO_{2\text{-}x}$ with its refractive index determined by the laser intensity [45]. The combination of the two media results in the local birefringence of the written pattern. By rotating and translating the substrate, spatially varying birefringence nanostructures are induced, of which the optical axis orientation is dependent on the incident laser polarization [46]. The writing depth is uniformly designed so that the metasurface works as a half-wave plate with a space-variant optical axis to achieve highly efficient phase modulation.

The polariscopic optical characterization images are employed to characterize the generated space-variant birefringence patterns of two stacked metasurfaces, as shown in Figs. 2(b) and 2(e). The periods of the sinusoidal patterns formed in the overlapped regions are determined by the difference of the periods of the metasurface pair, according to the definition of the space-variant phase $\kappa(x)$. Note that the two metasurfaces with identical periods [Fig. 2(e)] cancel the linear geometric phase of each other and yield a uniform transmission in the overlapped region. The orientations of the nanostructures of the two overlaid metasurfaces in the white dashed boxes in Figs. 2(b) and 2(e) are displayed in Figs. 2(c) and 2(f).

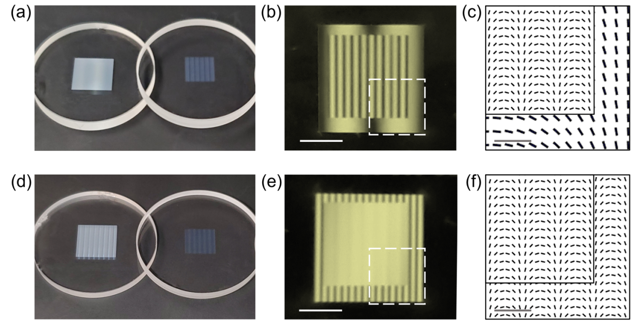

Fig. 2. Characterization of the metasurfaces embedded in silica glass. (a) and (d) Photographs of the metasurface pairs with periods of: (a) 8 mm (left, 8 mm × 8 mm pattern area), and 1 mm (right, 6 mm × 6 mm pattern area); and (d) 1 mm (left, 8 mm × 8 mm pattern area), and 1 mm (right, 6 mm × 6 mm pattern area), respectively. (b) and (e) Pseudo color photographs of the patterned areas of the overlaid metasurface pairs shown in (a) and (d) inserted between two crossed polarizers illuminated by a monochromatic source. Scale bars, 3 mm. (c) and (f) Optical axis distributions of the two overlaid metasurfaces in the white dashed boxes in (b) and (e). Scale bars, 1 mm.

The diffraction efficiency of the metasurface is defined as the ratio of the summed power of +1 and −1 orders to the total transmitted power after the metasurface, which is 92% measured by a laser power meter at a wavelength of 532 nm. The corresponding transmission efficiency (the ratio between the total transmitted power and the incident power) is as high as 96%.

B. Metasurface-Tuned Phase Retardation

The phase retardation of the output field is related to the periods of the metasurfaces along with the polarization orientation of the analyzer, according to Eq. (2). Here, we demonstrate the tunable phase retardation in the retardance images captured by a polarized camera when various metasurface pairs are applied. Figure 3(a) shows the experimental setup. The two metasurfaces are inserted between the sample and the objective (10 × /0.25 NA Olympus objective) with a homemade 3D-printed holder. MS_1 and MS_2 are centrally aligned and placed at distances of $z_1 = 3.6$ mm and $z_2 = 7$ mm with respect to the object. Fixed acute myeloid leukemia cells (SKNO-1) are illuminated with a 532 nm laser and imaged with a polarization CMOS camera (BFS-U3-51S5P-C, IMX250MZR, Teledyne FLIR), which contains interspersed polarized pixels with 0°, 45°, 90°, and 135° polarization orientations. Thus, four subframes of retardance images with a sequential phase retardation interval of 90° are obtained by deinterlacing a single shot captured by the polarized camera.

The four retardance images with a metasurface pair of various combination of periods: $\Lambda_1 = +\infty$ mm (no MS_1), $\Lambda_2 = 1$ mm; $\Lambda_1 = 8$ mm, $\Lambda_2 = 1$ mm; and $\Lambda_1 = 1$ mm, $\Lambda_2 = 1$ mm are presented in Figs. 3(b)–3(d), respectively. In the first two cases, since the two metasurfaces have different periods, their mismatching phase profiles form a nonuniform sinusoidal background, which indicates a spatially dependent phase retardation in the output images. The bright peaks of the fringe patterns correspond to a zero-phase retardation that leads to a constructive addition, while the dark valleys are associated with a π phase retardation that results in destructive interference. Determined by the difference of Λ_1 and Λ_2, the frequencies of the periodic sinusoidal background gradually decrease, as shown in Figs. 3(b)–3(d). The frequency

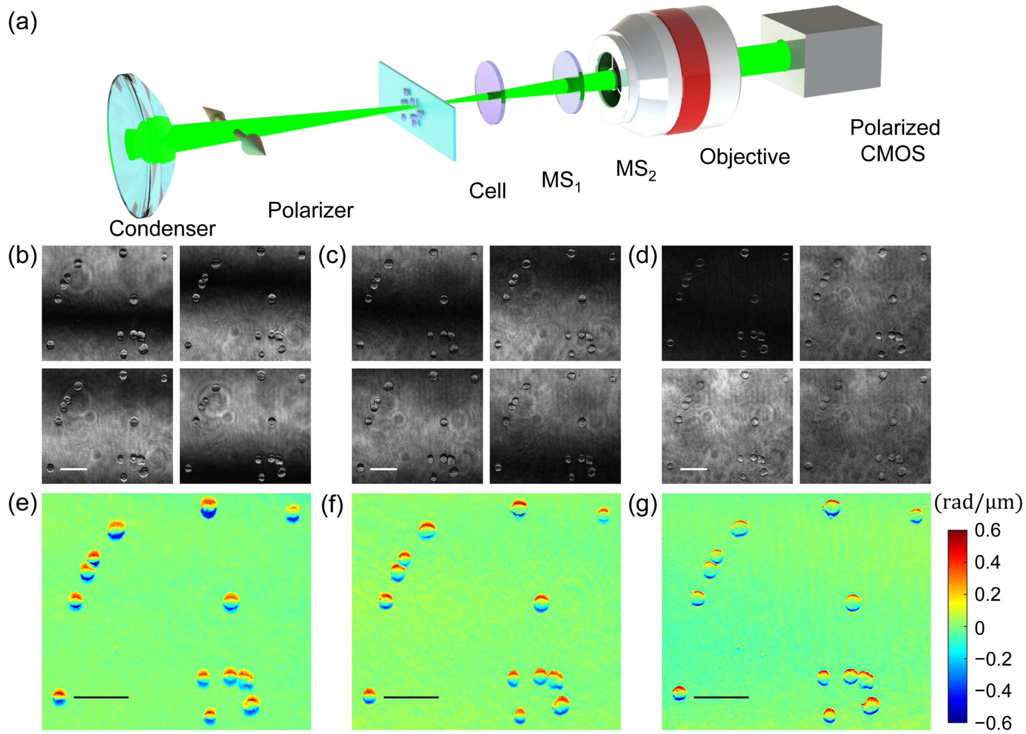

Fig. 3. Retardance images and QPGIs of SKNO-1 cells obtained with metasurface pair of various combination of periods. (a) Experiment setup. (b), (c), and (d) Simultaneously obtained four retardance images with different phase delays given various metasurface pairs. The periods of metasurfaces are: (b) $\Lambda_1 = +\infty$ mm (no MS$_1$), $\Lambda_2 = 1$ mm; (c) $\Lambda_1 = 8$ mm, $\Lambda_2 = 1$ mm; and (d) $\Lambda_1 = 1$ mm, $\Lambda_2 = 1$ mm. Scale bars, 50 μm. (e), (f), and (g) Calculated QPGI images of the cells by processing the images from (b), (c), and (d) with a generalized phase-stepping algorithm. Scale bars, 50 μm.

reaches zero in Fig. 3(d) when MS$_2$ perfectly cancels the phase gradient from MS$_1$, where the retardance images with uniform bias retardations controlled by the polarization orientation of the analyzer can be obtained. With a generalized phase-stepping algorithm, the phase gradient images [Figs. 3(e)–3(g)] are reconstructed given the retardance images with well-separated phase retardations. The lateral displacements Δ of the two replicas are related to the periods of the two metasurfaces and are measured to be 3.7 μm, 3.5 μm, and 1.9 μm in Figs. 3(e)–3(g), respectively.

With two identical metasurfaces, we obtain retardance images with spatially constant bias retardations, which are easier to interpret and require a simpler calculation for the phase gradient. Meanwhile, the lateral displacement is decoupled from the absolute positions of the two metasurfaces with respect to the object and only related to the relative distance d between them. This implies that if d is fixed, the position of the metasurface pair will not change the lateral displacement Δ_0, which can be designed to be optimal for the phase reconstruction. Therefore, in the following experiments, we employ two metasurfaces with the same period $\Lambda = 1$ mm.

C. QPGI with Tunable Resolution

We next verify the QPGI capability of our system with pure phase samples. A thin polymethyl methacrylate (PMMA) film with holes [Fig. 4(a)] is used as a calibration sample to confirm the accuracy of the phase quantification. See Section S3 of Supplement 1 for fabrication details. The phase gradient calculated with retardance images captured using two identical metasurfaces of $\Lambda = 1$ mm is presented in Fig. 4(b). The cross section and the thickness calculated from the phase gradient along the white dashed line in Fig. 4(b) are shown as the black and blue curves in Fig. 4(c). The thickness of the PMMA thin film characterized with our system is $\Delta\phi/[2\pi(n_{\mathrm{PMMA}} - n_{\mathrm{air}})]\lambda = 239$ nm, where $\Delta\varphi$ is the difference between the averaged phases within the areas with and without the PMMA thin film, $n_{\mathrm{PMMA}} = 1.4934$, $n_{\mathrm{air}} = 1$ are the refractive indices of PMMA and air, and $\lambda = 532$ nm is the working wavelength. The estimated thickness agrees with the sample surface measured by atomic force microscopy, as shown in Fig. S4 in Supplement 1.

The lateral displacement in the quantitative phase gradient reconstruction can be tuned by adjusting the distance between the two metasurfaces. To optimize the performance of our system, the QPGI of fixed MCF-7 human breast cancer cells is done when the two identical metasurfaces are separated by 5.1, 3.4, and 1.7 mm. Figures 4(d), 4(f) and 4(h) show the four retardance images with a lateral displacement Δ_0 of 2.7, 1.8, and 0.9 μm along the vertical direction, respectively. Because the metasurfaces are located closer to each other, the phase gradients [Figs. 4(e), 4(g), and 4(i)] of the objects yield better resolutions. Theoretically, the smaller the lateral displacement Δ_0 is, the more accurate the phase gradient and retrieved phase are. In practice, the phase accuracy is also limited by the SNR as well as the NA of the objective. A detailed numerical analysis is provided in Section S4 in Supplement 1.

D. QAPI

Finally, after optimizing the periods and displacement of the metasurfaces, we used two metasurfaces separated by 1.7 mm with identical periods of 1 mm to show the QAPI capability of the proposed technique. The bright field image of the object, SKNO-1 cells with Wright–Giemsa staining, is shown in Fig. 5(a). The

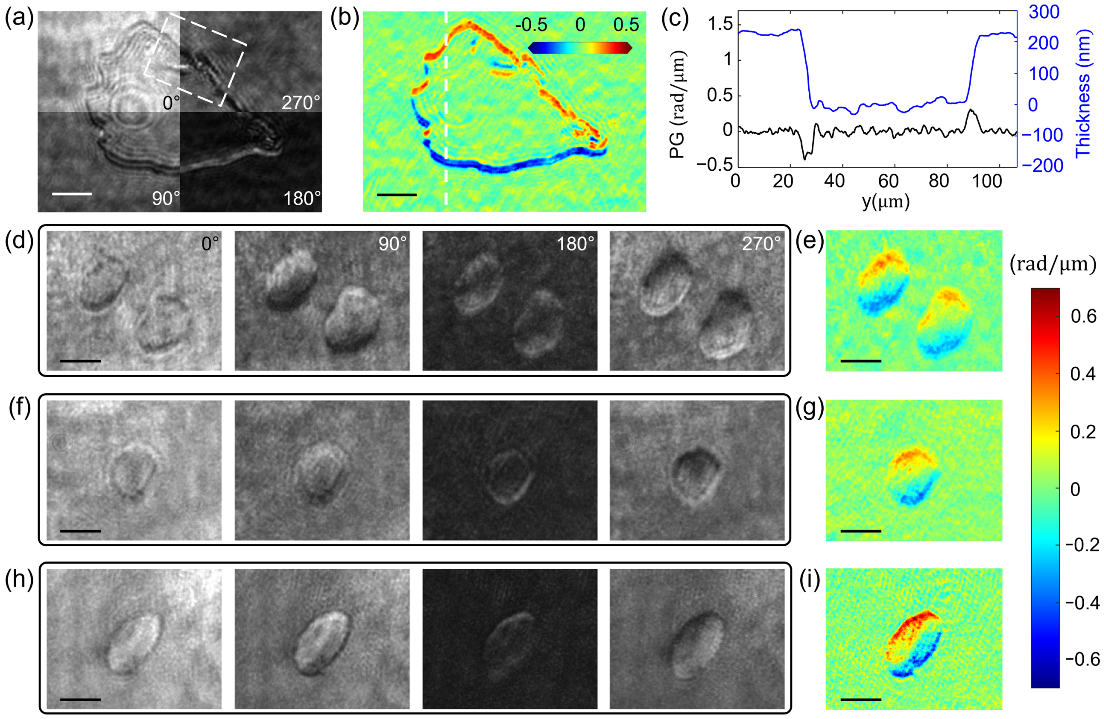

Fig. 4. QPGI of the calibration sample and MCF-7 cells with two metasurfaces of 1 mm periods separated by various distances. (a) Composite view of the four retardance images of the calibration sample, a PMMA thin film with a hole at the center. (b) Calculated QPGI of the calibration sample. Scale bars, 20 μm. (c) Cross-section and the thickness calculated from the phase gradient along the white dashed line in (b). (d), (f), and (h) Retardance images of MCF-7 cells with phase retardations of 0°, 90°, 180°, and 270° captured when the two metasurfaces are displaced by 5.1, 3.4, and 1.7 mm, respectively. (e), (g), and (i) Phase gradient images calculated with the retardance images from (d), (f), and (h). Scale bars, 20 μm.

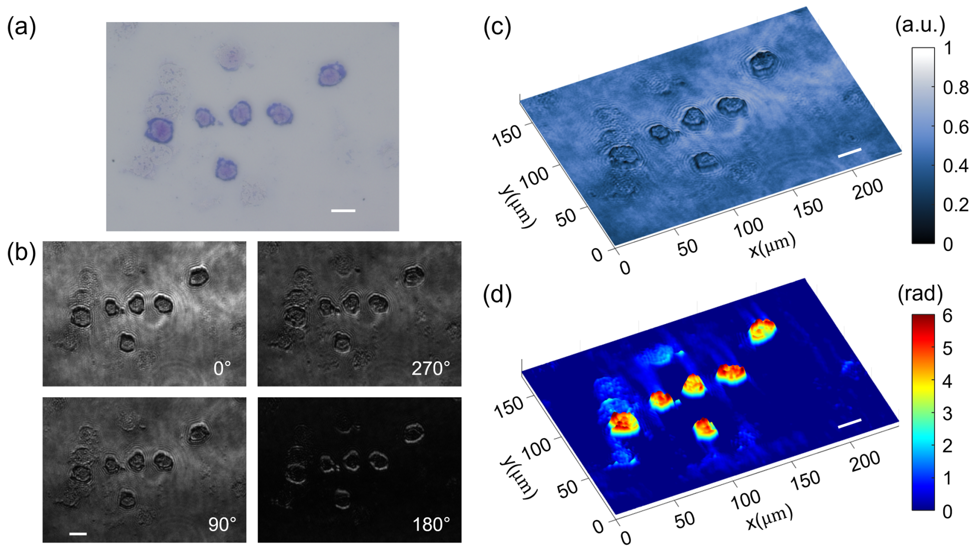

Fig. 5. Single-shot QAPI of stained SKNO-1 cells. (a) Bright field image of the cells. (b) Retardance images with phase retardation of 0°, 90°, 180°, and 270°. (c) and (d) Recovered amplitude and phase of the cells. Scale bars, 20 μm.

staining protocol can be found in Section S5 in Supplement 1. Figure 5(b) shows the four retardance images with phase retardations of 0°, 90°, 180, and 270° captured in a single shot. The phase gradient and amplitude of the object are calculated with Eqs. (4) and (6). The phase information is further retrieved by solving the l_1 total variation regularized problem in Eq. (5). The quantitative amplitude and phase images with 3D rendering of the recovered phase distribution are shown in Figs. 5(c) and 5(d), which simultaneously reveal stained features and surface profiles.

4. DISCUSSION AND CONCLUSION

The FOV of the proposed imaging system is limited by the size of the patterned area of the metasurfaces as well as the FOV of the microscope; in our system, the former is much larger than the latter. The resolution of the reconstructed quantitative phase images depends on the NA of the objective and the lateral displacement Δ between the two replicas, which is determined by the periods of the metasurfaces and the distance between them. A smaller displacement Δ results in better resolved phase reconstruction since a smaller Δ causes less blurring of the reconstructed field along the shearing direction. To enhance the resolution, a small Δ is desired, which, however results in a small numerator in the finite difference approximation in Eq. (4) and further leads to noisy reconstruction. An appropriately chosen Δ will keep the robustness of the phase recovery to noise during measurements without affecting the resolution too much (see Section S4 in Supplement 1).

The proposed reconstruction method performs a l_1 total variation regularized optimization by employing a sparsity prior on the second-order partial derivative of the object phase. While the method has shown effectiveness and efficiency in recovering the object phase for the class of objects we imaged, the reconstruction can be optimized for various types of scenes by applying appropriate regularizations and properly weighting them. For instance, the first-order total variation excels at preserving sharp edges, while the second-order total variation is better at resolving smooth transitions. A suitable combination of the two regularizers would lead to image restoration with superior quality under certain scenarios [47]. Additionally, deep learning, which has emerged as a powerful tool for data modeling and analysis, can enhance the quality of QPI [48] and solve the ill-posed inverse problem efficiently within a significantly reduced processing time [49,50].

In conclusion, we have proposed and demonstrated a single-shot QAPI method based on a pair of all-dielectric metasurfaces placed near any conjugate plane of the object. Compared to conventional or other metasurface-based QPI techniques, a main advantage of the proposed technique is the flexibility to place the metasurface pair without modifying existing setups. The retardance images can be formed if the metasurfaces are placed within close proximity of any conjugate plane of the object; e.g., in front of the image sensor or right beneath the specimen. Our method does not demand Fourier plane access, which typically comes at the expense of adding lengthy extension modules, or require precise alignment among components where bulky translational stages are usually inevitable. Note that the proposed metasurface pair can be miniaturized to a monolithic bilayer metasurface. The bilayer metasurface can be integrated on an image sensor to realize a plug-and-play QAPI camera that is compatible with various standard imaging systems. Directly writing the metasurface patterns into glass slides or petri dishes that hold specimens for examination provides another straightforward and user-friendly QAPI implementation. In addition, optical diffraction tomography can be combined with the metasurfaces-assisted QAPI system to achieve 3D volumetric refractive indexes of samples by scanning the illumination angles [51]. We expect our proposed scheme will provide much convenience for ultrafast QAPI of live specimens. Thanks to the compact configuration and simple implementation, the metasurface pair can be easily adapted to existing imaging systems, opening a new avenue for multimodal imaging.

Funding. Gordon and Betty Moore Foundation.

Acknowledgment. The authors would like to thank Putian He for taking the atomic force microscopy images. **Author contributions.** J. Zhou conceived the concept. Q. Wu developed the theoretical methods. J. Zhou and Q. Wu performed the experiment and analyzed the data. X. Chen and Y. Lo provided the biological cells. M. Lei contributed to the PMMA sample fabrication. Q. Wu wrote the manuscript and all authors revised the final manuscript. Z. Liu supervised this project.

Disclosures. The authors declare no conflicts of interest.

Data Availability. Data and codes underlying this work may be obtained from the corresponding author upon reasonable request.

Supplemental document. See Supplement 1 for supporting content.

REFERENCES

1. F. Zernike, “How I discovered phase contrast,” Science **121**, 345–349 (1955).
2. W. Lang, *Nomarski Differential Interference-Contrast Microscopy* (Carl Zeiss Oberkochen, 1982).
3. G. Popescu, *Quantitative Phase Imaging of Cells and Tissues* (McGraw-Hill Education, 2011).
4. R. Alford, H. M. Simpson, J. Duberman, G. C. Hill, M. Ogawa, C. Regino, H. Kobayashi, and P. L. Choyke, “Toxicity of organic fluorophores used in molecular imaging: literature review,” Mol. Imag. **8**, 354 (2009).
5. M. Mir, B. Bhaduri, R. Wang, R. Zhu, and G. Popescu, “Quantitative phase imaging,” Prog. Opt. **57**, 133–217 (2012).
6. Y. Park, C. Depeursinge, and G. Popescu, “Quantitative phase imaging in biomedicine,” Nat. Photonics **12**, 578–589 (2018).
7. G. A. Dunn and D. Zicha, “Phase-shifting interference microscopy applied to the analysis of cell behaviour,” Symp. Soc. Exp. Biol. **47**, 91–106 (1993).
8. C. Zuo, J. Li, J. Sun, Y. Fan, J. Zhang, L. Lu, R. Zhang, B. Wang, L. Huang, and Q. Chen, “Transport of intensity equation: a tutorial,” Opt. Laser Eng. **135**, 106187 (2020).
9. G. Zheng, R. Horstmeyer, and C. Yang, “Wide-field, high-resolution Fourier ptychographic microscopy,” Nat. Photonics **7**, 739–745 (2013).
10. L. Tian, X. Li, K. Ramchandran, and L. Waller, “Multiplexed coded illumination for Fourier ptychography with an LED array microscope,” Biomed. Opt. Express **5**, 2376–2389 (2014).
11. P. Marquet, B. Rappaz, P. J. Magistretti, E. Cuche, Y. Emery, T. Colomb, and C. Depeursinge, “Digital holographic microscopy: a noninvasive contrast imaging technique allowing quantitative visualization of living cells with subwavelength axial accuracy,” Opt. Lett. **30**, 468–470 (2005).
12. B. Bhaduri, C. Edwards, H. Pham, R. Zhou, T. H. Nguyen, L. L. Goddard, and G. Popescu, “Diffraction phase microscopy: principles and applications in materials and life sciences,” Adv. Opt. Photon. **6**, 57–119 (2014).
13. Y. Baek, K. Lee, J. Yoon, K. Kim, and Y. Park, “White-light quantitative phase imaging unit,” Opt. Express **24**, 9308–9315 (2016).
14. P. Bon, G. Maucort, B. Wattellier, and S. Monneret, “Quadriwave lateral shearing interferometry for quantitative phase microscopy of living cells,” Opt. Express **17**, 13080–13094 (2009).
15. S. Khadir, D. Andrén, R. Verre, Q. Song, S. Monneret, P. Genevet, M. Käll, and G. Baffou, “Metasurface optical characterization using quadriwave lateral shearing interferometry,” ACS Photon. **8**, 603–613 (2021).
16. P. Bouchal, L. Štrbková, Z. Dostál, R. Chmelík, and Z. Bouchal, “Geometric-phase microscopy for quantitative phase imaging of isotropic, birefringent and space-variant polarization samples,” Sci. Rep. **9**, 3608 (2019).
17. N. Yu, P. Genevet, M. A. Kats, F. Aieta, J.-P. Tetienne, F. Capasso, and Z. Gaburro, “Light propagation with phase discontinuities: generalized laws of reflection and refraction,” Science **334**, 333–337 (2011).
18. A. V. Kildishev, A. Boltasseva, and V. M. Shalaev, “Planar photonics with metasurfaces,” Science **339**, 1232009 (2013).
19. M. Khorasaninejad and F. Capasso, “Metalenses: versatile multifunctional photonic components,” Science **358**, eaam8100 (2017).
20. S. Wang, P. C. Wu, V.-C. Su, Y.-C. Lai, M.-K. Chen, H. Y. Kuo, B. H. Chen, Y. H. Chen, T.-T. Huang, J.-H. Wang, R.-M. Lin, C.-H. Kuan, T. Li, Z. Wang, S. Zhu, and D. P. Tsai, “A broadband achromatic metalens in the visible,” Nat. Nanotechnol. **13**, 227–232 (2018).
21. X. Hua, Y. Wang, S. Wang, X. Zou, Y. Zhou, L. Li, F. Yan, X. Cao, S. Xiao, D. P. Tsai, J. Han, Z. Wang, and S. Zhu, “Ultra-compact snapshot spectral light-field imaging,” Nat. Commun. **13**, 2732 (2022).
22. M. Khorasaninejad, F. Aieta, P. Kanhaiya, M. A. Kats, P. Genevet, D. Rousso, and F. Capasso, “Achromatic metasurface lens at telecommunication wavelengths,” Nano Lett. **15**, 5358–5362 (2015).
23. G. Zheng, H. Mühlenbernd, M. Kenney, G. Li, T. Zentgraf, and S. Zhang, “Metasurface holograms reaching 80% efficiency,” Nat. Nanotechnol. **10**, 308–312 (2015).
24. B. Xiong, Y. Xu, J. Wang, L. Li, L. Deng, F. Cheng, R.-W. Peng, M. Wang, and Y. Liu, “Realizing colorful holographic mimicry by metasurfaces,” Adv. Mater. **33**, 2005864 (2021).

25. S. Lan, X. Zhang, M. Taghinejad, S. Rodrigues, K.-T. Lee, Z. Liu, and W. Cai, “Metasurfaces for near-eye augmented reality,” ACS Photon. **6**, 864–870 (2019).
26. Y. Shi, C. Wan, C. Dai, Z. Wang, S. Wan, G. Zheng, S. Zhang, and Z. Li, “Augmented reality enabled by on-chip meta-holography multiplexing,” Laser Photon. Rev. **16**, 2100638 (2022).
27. H. Kwon, D. Sounas, A. Cordaro, A. Polman, and A. Alù, “Nonlocal metasurfaces for optical signal processing,” Phys. Rev. Lett. **121**, 173004 (2018).
28. A. Silva, F. Monticone, G. Castaldi, V. Galdi, A. Alù, and N. Engheta, “Performing mathematical operations with metamaterials,” Science **343**, 160–163 (2014).
29. Z. Wang, G. Hu, X. Wang, X. Ding, K. Zhang, H. Li, S. N. Burokur, Q. Wu, J. Liu, J. Tan, and C. W. Qiu, “Single-layer spatial analog meta-processor for imaging processing,” Nat. Commun. **13**, 1–10 (2022).
30. J. Zhou, H. Qian, C. F. Chen, J. Zhao, G. Li, Q. Wu, H. Luo, S. Wen, and Z. Liu, “Optical edge detection based on high-efficiency dielectric metasurface,” Proc. Natl. Acad. Sci. USA **116**, 11137–11140 (2019).
31. Y. Zhou, H. Zheng, I. I. Kravchenko, and J. Valentine, “Flat optics for image differentiation,” Nat. Photonics **14**, 316–323 (2020).
32. J. Zhou, H. Qian, J. Zhao, M. Tang, Q. Wu, M. Lei, H. Luo, S. Wen, S. Chen, and Z. Liu, “Two-dimensional optical spatial differentiation and high-contrast imaging,” Natl. Sci. Rev. **8**, nwaa176 (2021).
33. H. Kwon, E. Arbabi, S. M. Kamali, M. Faraji-Dana, and A. Faraon, “Computational complex optical field imaging using a designed metasurface diffuser,” Optica **5**, 924–931 (2018).
34. H. Kwon, E. Arbabi, S. M. Kamali, M. Faraji-Dana, and A. Faraon, “Single-shot quantitative phase gradient microscopy using a system of multifunctional metasurfaces,” Nat. Photonics **14**, 109–114 (2019).
35. E. Engay, D. Huo, R. Malureanu, A. I. Bunea, and A. Lavrinenko, “Polarization-dependent all-dielectric metasurface for single-shot quantitative phase imaging,” Nano Lett. **21**, 3820–3826 (2021).
36. J. Zhou, Q. Wu, J. Zhao, C. Posner, M. Lei, G. Chen, J. Zhang, and Z. Liu, “Fourier optical spin splitting microscopy,” Phys. Rev. Lett. **129**, 020801 (2022).
37. S. Pancharatnam, “Generalized theory of interference and its applications,” in *Proc. Indiana Acad. Sci.* (1956), Vol. **44**, pp. 398–417.
38. M. V. Berry, “Quantal phase factors accompanying adiabatic changes,” Proc. R. Soc. A **392**, 45–57 (1984).
39. K. Creath, “V phase-measurement interferometry techniques,” Prog. Opt. **26**, 349–393 (1988).
40. J. Greivenkamp, “Generalized data reduction for heterodyne interferometry,” Opt. Eng. **23**, 350–352 (1984).
41. M. Arnison, C. Cogswell, N. Smith, P. Fekete, and K. Larkin, “Using the Hilbert transform for 3D visualization of differential interference contrast microscope images,” J. Microsc. **199**, 79–84 (2000).
42. M. Strassberg, Y. Shevtsova, D. Kamel, K. Wagoner-Oshima, H. Zhong, and M. Xu, “Single-shot quantitative phase imaging with polarization differential interference contrast,” Appl. Phys. Lett. **119**, 173702 (2021).
43. J. Matias Di Martino, J. L. Flores, F. Pfeiffer, K. Scherer, G. A. Ayubi, and J. A. Ferrari, “Phase retrieval from one partial derivative,” Opt. Lett. **38**, 4813–4816 (2013).
44. S. Boyd, “Distributed optimization and statistical learning via the alternating direction method of multipliers,” Found. Trends Mach. Learn. **3**, 1–122 (2010).
45. Y. Shimotsuma, P. G. Kazansky, J. Qiu, and K. Hirao, “Self-organized nanogratings in glass irradiated by ultrashort light pulses,” Phys. Rev. Lett. **91**, 247405 (2003).
46. M. Beresna, M. Gecevičius, P. G. Kazansky, and T. Gertus, “Radially polarized optical vortex converter created by femtosecond laser nanostructuring of glass,” Appl. Phys. Lett. **98**, 201101 (2011).
47. S. Didas, S. Setzer, and G. Steidl, “Combined ℓ_2 data and gradient fitting in conjunction with ℓ_1 regularization,” Adv. Comput. Math. **30**, 79–99 (2009).
48. Y. Jo, H. Cho, S. Y. Lee, G. Choi, G. Kim, H. S. Min, and Y. Park, “Quantitative phase imaging and artificial intelligence: a review,” IEEE J. Sel. Top. Quantum Electron. **25**, 6800914 (2019).
49. A. Sinha, J. Lee, S. Li, and G. Barbastathis, “Lensless computational imaging through deep learning,” Optica **4**, 1117–1125 (2017).
50. Y. Rivenson, Y. Zhang, H. Günaydın, D. Teng, and A. Ozcan, “Phase recovery and holographic image reconstruction using deep learning in neural networks,” Light Sci. Appl. **7**, 17141 (2018).
51. S. Chowdhury, M. Chen, R. Eckert, D. Ren, F. Wu, N. Repina, and L. Waller, “High-resolution 3D refractive index microscopy of multiple-scattering samples from intensity images,” Optica **6**, 1211–1219 (2019).